Available online at www.sciencedirect.com
SCIENCE DIRECT®
Journal of Applied Geophysics 54 (2003) 369–389
JOURNAL OF APPLIED GEOPHYSICS
www.elsevier.com/locate/jappgeo

Decoupled elastic prestack depth migration ☆

Alexander Druzhinin *

British Geological Survey, Murchison House, West Mains Road, Edinburgh EH9 3LA, UK

Abstract

This paper presents a new decoupled form of the formula for common-shot or common-receiver amplitude-preserving elastic prestack depth migration (PreSDM), which can be used for estimating angle-dependent elastic reflection coefficients in laterally inhomogeneous anisotropic media. The multi-shot or multi-receiver extension of this formula is suitable for automated prestack amplitude-versus-angle (AVA) elastic inversion of ocean-bottom cable (OBC), walkaway VSP (WVSP) or standard towed-cable data at any subsurface location. The essence of the theory is a systematic application of the stationary-phase principle and high-frequency approximations to the basic elastic Green's theorem. This leads to nonheuristic explicit wave mode decoupling and scalarization of vector PreSDM. Used in combination, ray-trace and finite-difference (FD) eikonal solvers create a useful tool to calculate accurate Green's function travel time and amplitude maps. Examples of synthetic OBC data and applications to field WVSP data show that the new imaging technique can produce a clear multi-mode elastic image.

Keywords: Elastic imaging; Decoupling; Stationary-phase principle; Converted waves; Anisotropy

1. Introduction

In vector seismic processing, it is common practice to enhance strongly polarized wave modes prior to prestack depth migration (PreSDM) (e.g. Dillon et al., 1988; Hou and Marfurt, 2002). However, migration artifacts due to incomplete wavefield separation often make it difficult to interpret the migrated amplitudes in terms of reflecting surface excitations. To overcome this, we may formulate the vector PreSDM procedure as a coupled wavefield reconstruction problem (Sena and Toksöz, 1993; Hokstad, 2000) based on the Kirchhoff–Helmholtz (KH) elastic modeling theory (Wapenaar and Berkhout, 1989; Druzhinin et al., 1998; Schleicher et al., 2001). In theory, because of the elastic imaging principle (Kuo and Dai, 1984) separation of wave modes occurs implicitly in the existing coupled KH migration algorithms. In practice, however, minimization of cross-talk energy between modes is not possible on account of cross-component noise (Zhe and Greenhalgh, 1997). For example, in 3D inhomogeneous anisotropic media strong frequency dependent coupling can occur between the two shear modes. This makes the anisotropic migration process considerably more difficult. To achieve some degree of robustness, a number of ad hoc weighting functions have been incorporated into multi-component stacking procedures (Milkereit and Spencer, 1987; Takahashi, 1995; Kennett, 2000). These arrival-angle directivity functions accomplish a partial wave mode selection by increasing the vector signal-to-noise ratio.

☆ Presented at the 10th International Workshop on Seismic Anisotropy, Tutzing, Germany, 14–19 April 2002.

* Tel.: +44-131-650-0435; fax: +44-131-667-1877.
E-mail address: adrou@bgs.ac.uk (A. Druzhinin).

0926-9851/$ - see front matter © 2003 Elsevier B.V. All rights reserved.
doi:10.1016/j.jappgeo.2003.03.001

The purpose of this paper is to show that it is possible to achieve a complete rigorous wavefield separation during migration whilst avoiding the limitations of the migration schemes mentioned above. As with acoustic PreSDM (Docherty, 1991), a non-heuristic, systematic approach based on the stationary-phase principle (Bleistein, 1984) is applied to the basic KH integral. To create instantaneous scalar projections, we use complex-trace transformations of input data (Vidale, 1986) as well as arrival-angle and polarization stacking weights in addition to the amplitude weights implicit in true-amplitude PreSDM. The paper is focused on a rigorous derivation of a true-amplitude migration formula for mode-converted data. It does not address the estimation of parameters for the anisotropic migration model.

2. Basic notations

All lower-case Roman indices take values 1, 2 and 3, and the summation rule over repeated indices is employed throughout this paper. Cartesian components of the vector $\boldsymbol{p}$ will be denoted by p_k; 3×3 matrices will be denoted either by $\mathbf{g}$ or g_{ij}; ∂_k will designate the spatial derivative $\partial/\partial x_k$ with respect to Cartesian coordinates x_k of the current point; $C_{ijkl} = C_{jikl} = C_{ijlk} = C_{klij}$ will denote the Cartesian components of the fourth rank elastic stiffness tensor $\mathbf{C}$. The point Q will be specified by the position vector $\boldsymbol{r}(Q) = \{x_k(Q)\}$; $r(Q,R) = |\boldsymbol{r}(Q) - \boldsymbol{r}(R)|$ will denote the distance between the points Q and R. The time derivative $\partial f/\partial t$ will be denoted by $\dot{f}$. The symbol O will indicate the asymptotic estimate. We shall deal with the steady-state wavefield $\boldsymbol{u}(Q,t) = \boldsymbol{u}(Q)\exp(-i\omega t)$ as a function of the time t and spatial variables $\boldsymbol{r}(Q)$ ($i = \sqrt{-1}$ and ω is the frequency). The time factor $\exp(-i\omega t)$ will be suppressed henceforth from all field quantities.

3. Formulation of the problem

Referring to Fig. 1, we formulate the migration problem of recovering subsurface structure in the region V under consideration. This region is occupied by an inhomogeneous and anisotropic medium described by the fourth rank elastic stiffness tensor $\mathbf{C}(Q)$

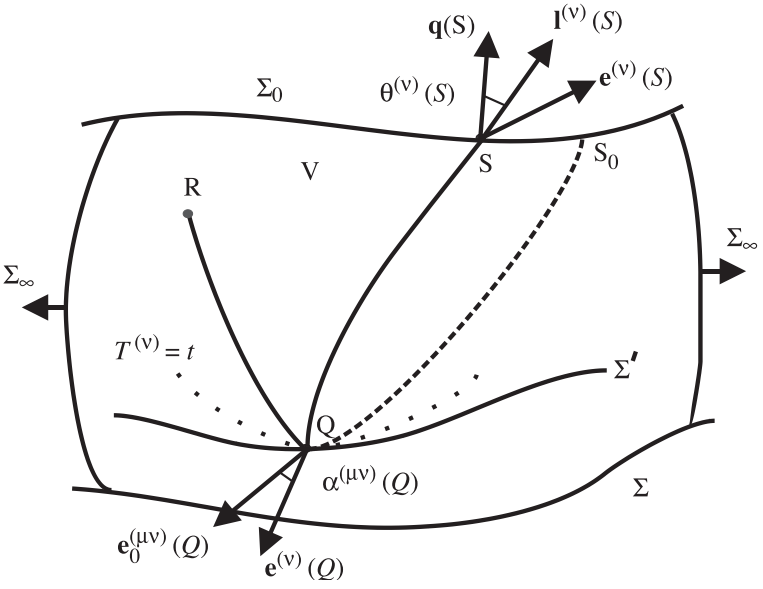

Fig. 1. Geometry of the problem: $\boldsymbol{e}^{(\nu)}$ is the plane-wave unit polarization vector of the νth wave mode associated with the two-point emerging ray path SQ, $\boldsymbol{e}_0^{(\mu\nu)}$ is the plane-wave unit polarization vector of the μth wave mode associated with the specular (say, reflected) ray RQS_0 with the origin at R, $\theta^{(\nu)}(S)$ is the acute angle the emerging ray SQ makes with the normal to Σ_0 at S.

and the mass density $\rho(Q)$. It is bounded internally by the surface $\Sigma_0+\Sigma$, and externally by a large surface Σ_∞, where Σ_0 denotes the acquisition surface and Σ the material discontinuity surface (e.g. bottom reflector). Let $\partial V=\Sigma_0+\Sigma+\Sigma_\infty$ be the boundary of the volume V with outward pointing unit normal $\boldsymbol{q}$, as shown in Fig. 1. The spherical or cylindrical interface Σ_∞ closes the target zone as $r_\infty\rightarrow\infty$, where r_∞ measures radial distance. We have many multi-component records of the displacement vector $\boldsymbol{u}(S,R,t)$ as a function of time t. These data are recorded at observation points R in the borehole (walkaway VSP, WVSP) or on the sea floor (ocean-bottom cable, OBC), each from different source positions S on Σ_0. In addition, streamer data $u(S,R,t)$ may be available for the source and receiver points S and R above the sea floor. Note that the WVSP measurements could be transformed into reverse VSP data, acquired with a down-hole source (DHS) at point R and a moving receiver at S, through the principle of reciprocity valid for elastic waves and marine observations (Mittet and Hokstad, 1995). We shall assume that special conditions, known as the radiation conditions (Wapenaar and Berkhout, 1989), are imposed on the far field behaviour of the displacement and traction vectors, so that the energy flux through the surface Σ_∞ will always be in the outward direction. The overall aim is to retrieve all material discontinuities bounded by the surface ∂V via downward continuation of the observed displacement vector into the target region. In doing so, we will explore special imaging conditions for outgoing elastic waves propagating in the region V.

4. Theoretical background

4.1. Basic integral theorem

Applying the elasto-dynamic Green's theorem (first integral formula) to the steady-state wavefield $\boldsymbol{u}(Q,t)$ in the volume V without body forces produces (Wapenaar and Berkhout, 1989)

$$u_m(Q)=-\int_{\Sigma_0+\Sigma}\{q_j(S)C_{ijkl}(S)[u_i(S,R)\partial_k g_{lm}(S,Q)-g_{im}(S,Q)\partial_k u_l(S,R)]\mathrm{d}\sigma(S)\},\quad Q\in V \quad (1)$$

Here, $u_i(S,R)$ is the ith component of the steady-state displacement vector $\boldsymbol{u}(S,R,\omega)$, q_j is the jth component of the unit normal to the surface ∂V, $C_{ijkl}(S)$ are the elastic parameters of the medium at the point S, and $\mathrm{d}\sigma$ is an infinitesimal area element on ∂V. In Eq. (1), the Green's displacement tensor $g_{im}(S,Q)$ represents the displacement component at S in the direction of the x_m-axis due to a concentrated body force applied at the point Q in the direction of the x_i-axis. For homogeneous boundary conditions, the reciprocity relation $g_{im}(S,Q)=g_{mi}(Q,S)$ is satisfied. Knowing the boundary values $\boldsymbol{u}(S,R,t)$ and $\nabla_S\boldsymbol{u}(S,R,t)$ of the wavefield and its spatial gradient, we can calculate the total wavefield inside V from Eq. (1).

4.2. Mode expansions

Let the observed frequency-domain wavefield $\boldsymbol{u}$ be decomposed in the form (Druzhinin et al., 1998)

$$\boldsymbol{u}=\sum_{\mu=1}^{M}\boldsymbol{u}^{(\mu)} \quad (2)$$

with terms

$$\boldsymbol{u}^{(\mu)}=\boldsymbol{a}^{(\mu)}u^{(\mu)}, \quad (3)$$

where

$$u^{(\mu)}=A^{(\mu)}\exp(i\varphi^{(\mu)}) \quad (4)$$

and the index $\mu=1, 2,\ldots, M$ corresponds to the arrivals of various elementary propagating wave modes. For example, M may account for various types of reflected/transmitted waves caused by (possibly) different interfaces (Reiter et al., 1991; Červený, 2001). Eq. (3) is the well-known vector complex-trace representation (Vidale, 1986), in which the attributes $\boldsymbol{a}^{(\mu)}$, $A^{(\mu)}$ and $\varphi^{(\mu)}$ are, respectively, the polarization, amplitude and phase functions of the μth wave mode. In the high-frequency limit (e.g. Chapman and Coates, 1994), the phase function becomes $\varphi^{(\mu)}=\omega\tau^{(\mu)}$ and is expressed in terms of the travel time function $\tau^{(\mu)}$ corresponding to primary and multiple reflections, converted waves, etc. Eq. (2) is the implicit representation of the fundamental superposition principle based on the linearity property of the elasto-dynamic

equations of motion (Wapenaar and Berkhout, 1989; Červený, 2001).

Similarly, one can introduce the following dyadic frequency-domain Green's eigenvector expansion (Ben-Menahem et al., 1991; Druzhinin et al., 1998)

$$g_{im} = \sum_{v=1}^{N} g^{(v)} e_i^{(v)} e_m^{(v)} \tag{5}$$

by summation over different arrivals of N elementary wave modes

$$g^{(v)} = G^{(v)} \exp(s\ i\Phi^{(v)}), \quad s = \pm 1 \tag{6}$$

with the amplitude and phase functions $G^{(v)}$ and $\Phi^{(v)}$, respectively. In Eq. (5), $\boldsymbol{e}^{(v)}$ is the unit polarization vector and N accounts for Green's function far-field terms, coupled terms and multiples if any (Reiter et al., 1991). In one-way back propagation or migration, we use the advanced or anti-causal Green's function by setting $s=-1$ in Eq. (6). In the simple case of a smoothly varying background medium and a far-field limit within the domain V, the superscripts $v,\mu=1, 2, 3$ refer to three wave types corresponding to one quasi-P and two quasi-shear wave modes (Ben-Menahem et al., 1991; Chapman and Coates, 1994). In this case, the polarizations $\boldsymbol{e}^{(v)}$, the amplitudes $G^{(v)}$, and the phase functions $\Phi^{(v)}=\omega T^{(v)}$ may be determined from the Christoffel's equation, the transport equation, and the eikonal equation for the main component of the wavefield (Červený, 2001). Concerning amplitude computations, see also Eqs. (A1) and (B3).

4.3. Downward continuation

Substituting expansions (2) and (5) into Eq. (1) and taking into account expressions (3), (4) and (6) along with the high-frequency approximations (Schleicher et al., 2001)

$$\partial_k \boldsymbol{u}^{(\mu)} \approx i\omega \boldsymbol{u}^{(\mu)} \partial_k \tau^{(\mu)} \tag{7}$$

and

$$\partial_k g_{im} \approx i\omega \sum_{v=1}^{N} g^{(v)} e_i^{(v)} e_m^{(v)} \partial_k T^{(v)} \tag{8}$$

gives rise to the following multi-mode downward continuation equation

$$\boldsymbol{u}(Q) \approx \sum_{\mu,v} \boldsymbol{u}^{(\mu v)}(Q) \tag{9}$$

with vector terms

$$\boldsymbol{u}^{(\mu v)}(Q) = i\omega \int_{\Sigma_0+\Sigma} \{\boldsymbol{e}^{(v)}(Q) \Psi^{(\mu v)}(S,Q,R) A^{(\mu)}(S,R) \times G^{(v)}(S,Q) \exp[i\varphi^{(\mu v)}(S,Q,R)] \mathrm{d}\sigma(S)\}, \tag{10}$$

where

$$\phi^{(\mu v)}(S,Q,R) = \omega[\tau^{(\mu)}(S,R) - T^{(v)}(S,Q)] \tag{11}$$

and

$$\Psi^{(\mu v)}(S,Q,R) = q_j(S) C_{ijkl}(S) \times [e_l^{(v)}(S) a_i^{(\mu)}(S) \partial_k T^{(v)}(S,Q) + e_i^{(v)}(S) a_l^{(\mu)}(S) \partial_k \tau^{(\mu)}(S,R)] \tag{12}$$

Integral (9) over the surface Σ_0 is the explicit one-way KH downward continuation formula for multi-mode reverse-time extrapolation in the common-receiver wave-mode attribute domain. It is consistent with the concept of reflection/transmission operators in composite regions (Kennett, 1984), which bears a formal resemblance to the ray-theory decomposition of a field into a set of ray contributions (Červený, 2001). Hence, the full suite of elastic wave interactions can be followed by compounding the operators (10). The frequency-weave number $(\omega - k)$ coupled version of formula (10) was derived by Wapenaar and Berkhout (1989). A similar time-domain formula was obtained by Kuo and Dai (1984) for one-way propagation in isotropic media. It was extended by Sena and Toksöz (1993) to anisotropic media and adapted to marine observations by Hokstad (2000). These papers ignore the integral (9) over the surface Σ simply by selecting appropriate wave modes at the pre-processing stage. In contrast to previous studies (Kuo and Dai, 1984; Sena and Toksöz, 1993), the use of Eq. (10) does not depend on whether or not the surface Σ_0 is free since the boundary condition $C_{ijkl}(S)\partial_k u_l(S, R)=0$ is not used. Hence, Eq. (10) is suitable for recursive downward continuation of arbitrary data in multi-layered media.

4.4. Stationary-phase conditions

According to the stationary-phase principle (Bleistein, 1984; Schleicher et al., 2001), the Green's function isochrone surface $T^{(\nu)}=t$ must be tangent to the data-space isochrone surface $\tau^{(\mu)}=t$ at the stationary point(s) S of the boundary surface ∂V. Conventionally, we select upgoing waves by omitting downgoing energy at ∂V (Docherty, 1991). Since the major contributions to the surface integral (10) occur at locations where the phase is stationary, we have

$$\partial_k \tau^{(\mu)}(S,R) = \partial_k T^{(\nu)}(S,Q), \quad S\in\Sigma_0 \tag{13}$$

and

$$\partial_k \tau^{(\mu)}(S,R) = -\partial_k T^{(\nu)}(S,Q), \quad S\in\Sigma. \tag{14}$$

Condition (13) picks out the point S on the upper surface Σ_0 where the direction of the specular upgoing ray path SR is coincident with the direction of the upgoing ray path SQ. Likewise, condition (14) is satisfied on the lower surface Σ where the direction of the specular upgoing ray path SR is opposite to the direction of the downgoing ray path SQ. Note that Docherty (1991) adopts less stringent stationary-phase conditions on Σ by assuming that $q_i\partial_i\tau^{(\mu)}(S,R)=-q_i\partial_i T^{(\nu)}(S,Q)$.

From Eqs. (13) and (14) it follows that

$$\boldsymbol{a}^{(\mu)}(S) = \begin{cases} \boldsymbol{e}^{(\nu)}(S) & S\in\Sigma_0 \\ -\boldsymbol{e}^{(\nu)}(S) & S\in\Sigma \end{cases} \tag{15}$$

Now it is clear that the integral (9) over the surface Σ vanishes due to conditions (14) and (15). Moreover, we note that (Schleicher et al., 2001)

$$\begin{aligned} &q_j(S)C_{ijkl}(S)e_i^{(\nu)}(S)a_l^{(\mu)}(S)\partial_k T^{(\nu)}(S,Q) \\ &\quad = \rho(S)q_j(S)v_j^{(\nu)}(S) = \rho(S)v^{(\nu)}(S)\cos\theta^{(\nu)}(S), \end{aligned} \tag{16}$$

where $v_j^{(\nu)}$ is the jth component of the group velocity vector $\boldsymbol{v}^{(\nu)}$ corresponding to the νth Green's function wave mode (Ben-Menahem et al., 1991; Červený, 2001), $v^{(\nu)}=|\boldsymbol{v}^{(\nu)}|$ is the group velocity, and $\theta^{(\nu)}=\cos^{-1}(\boldsymbol{l}^{(\nu)}\cdot\boldsymbol{q})$ is the acute angle between the ray direction vector $\boldsymbol{l}^{(\nu)}=\boldsymbol{v}^{(\nu)}/v^{(\nu)}$ and the normal vector $\boldsymbol{q}$ (Fig. 1).

Finally, combining Eqs. (13)–(16), and taking into account Eqs. (2)–(4), a stationary-phase approximation of expansion (9) yields

$$\boldsymbol{u}(Q,\xi) \approx \sum_{\nu=1}^{N} \boldsymbol{u}^{(\nu)}(Q,\xi), \quad \xi=\omega,t, \tag{17}$$

with vector terms

$$\begin{aligned} \boldsymbol{u}^{(\nu)}(Q,\omega) = 2i\omega \int_{\Sigma_0} &\boldsymbol{e}^{(\nu)}(Q)u^{(\nu)}(S,R,\omega) \\ &g^{(\nu)}(S,Q)\Psi^{(\nu)}(S,Q)\mathrm{d}\sigma(S) \end{aligned} \tag{18}$$

or

$$\begin{aligned} \boldsymbol{u}^{(\nu)}(Q,t) = 2\int_{\Sigma_0} &\dot{\boldsymbol{u}}^{(\nu)}[S,R,t+T^{(\nu)}(S,Q)] \\ &\times G^{(\nu)}(S,Q)\Psi^{(\nu)}(S,Q)\mathrm{d}\sigma(S), \end{aligned} \tag{19}$$

where

$$\dot{\boldsymbol{u}}^{(\nu)}(S,R,t) = \boldsymbol{e}^{(\nu)}(Q)\dot{u}^{(\nu)}(S,R,t), \tag{20}$$

$$u^{(\nu)}(S,R,\xi) = \left(\boldsymbol{u}(S,R,\xi)\cdot\boldsymbol{e}^{(\nu)}(S)\right), \tag{21}$$

$$\Psi^{(\nu)}(S,Q) = \rho(S)v^{(\nu)}(S)\cos\theta^{(\nu)}(S), \tag{22}$$

and the function $g^{(\nu)}(S,Q)$ is defined by Eq. (6) with $s=-1$. Eq. (18) is a high-frequency approximation of the back-propagated wavefield that does not require the wave-mode expansion (2) or the integration over the reflector Σ. Even though this equation and its time-domain counterpart (19) are still applicable to elastic wave propagation in general anisotropic media, they have the very appealing form of a multiple-weighted reverse-time (back propagated) diffraction stack of the transformed data given by Eq. (20) (Tygel et al., 1993). The factor $\psi^{(\nu)}$ (Eq. (22)) and amplitude scaling terms embody the effects of geometrical spreading, transmission loss, and KH obliquity. With a slightly different meaning of input quantities involved, this resembles the common-receiver acoustic KH datuming formula (Docherty, 1991) due to the stationary-phase conditions (Eqs. (13)–(15)) and the identity (Eq. (16)).

4.5. Decoupled migration

To derive decoupled imaging conditions, let us define the following scalar product

$$u^{(\mu\nu)}(Q,\xi) = \left(\boldsymbol{u}(Q,\xi)\cdot\boldsymbol{e}_0^{(\mu\nu)}(Q)\right), \tag{23}$$

where the transformed wavefield $\boldsymbol{u}(Q,\xi)$ is given by Eq. (17) and $\boldsymbol{e}_0^{(\mu\nu)}(Q)$ is the unit polarization vector corresponding to a specular νth outgoing wave at point Q, due to the incident μth wave for the ray path RQ propagating from receiver R (Schleicher et al., 2001). Substituting Eq. (17) for $\boldsymbol{u}(Q,\omega)$ and noting that $(\boldsymbol{e}^{(\eta)}(Q)\cdot\boldsymbol{e}_0^{(\mu\nu)}(Q)) \approx 0$ when $\eta\neq\nu$ gives

$$u^{(\mu\nu)}(Q,\omega) \approx 2i\omega \int_{\Sigma_0} u^{(\nu)}(S,R,\omega) g^{(\nu)}(S,Q) \Psi^{(\nu)}(S,Q)\Omega^{(\mu\nu)}(Q)\mathrm{d}\sigma(S) \tag{24}$$

with

$$\Omega^{(\mu\nu)}(Q) = (\boldsymbol{e}^{(\nu)}(Q)\cdot\boldsymbol{e}_0^{(\mu\nu)}(Q)) = \cos\alpha^{(\mu\nu)}(Q) \tag{25}$$

The new obliquity factor $\Omega^{(\mu\nu)}$(Eq. (25)) plays a very important role in the wave-mode decoupling process. Similar to the arrival-angle weight empirically derived by Takahashi (1995), it enhances the contribution of the specular point as $\alpha^{(\mu\nu)}\to 0$ and suppresses false contributions far from that point. Since the vector $\boldsymbol{e}_0^{(\mu\nu)}(Q)$ is the expected polarization direction for the scattering point Q, the factor $\Omega^{(\mu\nu)}$ can be thought of as a polarization filter that minimizes the projection of the displacement vector at Q onto the plane with normal $\boldsymbol{e}_0^{(\mu\nu)}(Q)$. For instance, this filter should handle the isotropic shear-wave coupling problem because the polarization direction of the SV-wave is orthogonal to that of the SH-wave.

Bearing in mind the analogy with acoustic KH migration (Docherty, 1991), the decoupled imaging condition may be written as

$$I^{(\mu\nu)}(Q,t) = \int_{-\infty}^{+\infty} H(\omega)\exp(-i\omega t)\frac{u^{(\mu\nu)}(Q,\omega)}{u^{(\mu)}(R,Q)}\mathrm{d}\omega, \quad t\to 0, \tag{26}$$

where $I^{(\mu\nu)}(Q,0)$ is the migrated image at the target point Q, the function $u^{(\mu\nu)}(Q,\omega)$ is determined from Eq. (24), $u^{(\mu)}(R,Q)$ is the incident wavefield defined by Eq. (4), and $H(\omega)$ is the frequency-domain window function which emphasizes the band limited nature of observed records.

Following Červený (2001), we construct the specular ray RQS_0 with ray termination points R and $S_0\in\Sigma_0$ (Fig. 1). This allows us to define the amplitude-normalized plane-wave reflection/transmission coefficient $K^{(\mu\nu)}(Q)$ for our choice of incident and outgoing wave modes (Schleicher et al., 2001). It can be shown that (cf. Appendix B)

$$K^{(\mu\nu)}(Q) \approx \sec\theta^{(\nu)}(S_0)\lim_{t\to 0} I^{(\mu\nu)}(Q,t)/\dot{f}(t), \tag{27}$$

where $f(t)\leftrightarrow F(\omega)$ denotes the wavelet function of the data $\boldsymbol{u}(S,R,\omega)$ after zero-phase deconvolution. It is assumed that deconvolution is performed using the window function $H(\omega)$ and the original source signature $f_0(t)\leftrightarrow F_0(\omega)$. The derivation in Appendix B proves that Eq. (26) is the rigorous KH elastic imaging condition since no heuristic assumptions have so far been made.

Substituting Eq. (19) into Eq. (27) and invoking the well-known property of the δ-function

$$\frac{1}{2\pi}\int_{-\infty}^{+\infty} i\omega\,\exp(-i\omega t)\mathrm{d}\omega = \dot{\delta}(t) \tag{28}$$

we have

$$K^{(\mu\nu)}(Q) = \frac{4\pi}{A^{(\mu)}(R,Q)} \times \int_{\Sigma_0}\left(\dot{\boldsymbol{u}}_0[S,R,t=\tau^{(\mu\nu)}(S,Q,R)]\cdot\boldsymbol{e}^{(\nu)}(S)\right) \times G^{(\nu)}(S,Q)\Psi^{(\nu)}(S,Q)\Omega^{(\mu\nu)}(Q)\mathrm{d}\sigma(S), \tag{29}$$

where $\tau^{(\mu\nu)}(S,Q,R)=\tau^{(\mu)}(R,Q)+T^{(\nu)}(S,Q)\equiv\tau^{(\mu\nu)}$ is the travel time along the composite diffracted ray path SQR (Fig. 1), $\dot{\boldsymbol{u}}_0(S,R,t)$ is the input data $\dot{\boldsymbol{u}}_0(S,R,t)$ after source deconvolution using the filter $i\omega H(\omega)F_0(\omega)$ according to Eq. (27), the ray-theory amplitudes $G^{(\nu)}(S,Q)$ and $A^{(\mu)}(R,Q)$ are specified by Eqs. (A1) and (B3), and the obliquity factors $\Psi^{(\nu)}(S,Q)$ and $\Omega^{(\mu\nu)}(Q)$ are given by Eqs. (22) and (25), respectively.

Eq. (29) is a common-receiver true-amplitude elastic KH migration formula that can be used for an automated amplitude-versus-angle (AVA) inversion at every subsurface location (cf. Appendix C). It provides a true angle-dependent reflection coefficient (not a

Table 1
Elastic VTI parameters of the Moreni model with the parameter $\gamma = 0$

Layer number	V_p (km/s)	V_s (km/s)	ρ (g/cm^3)	ε	δ
1	1.50	0.000	1.00	0.0000	0.0000
2	1.60	0.250	1.85	0.0000	0.0000
3	1.85	0.462	2.00	0.0930	0.0300
4	1.90	0.500	2.10	0.1260	0.0350
5	2.20	0.880	2.30	0.1372	0.0400
6	2.60	1.130	2.10	0.1944	0.0600
7	2.40	0.960	2.30	0.0000	0.0000
8	2.80	1.220	2.25	0.2182	0.0700
9	2.70	1.230	2.40	0.1720	0.0600
10	3.00	1.500	2.30	0.0000	0.0000
11	2.60	1.180	2.20	0.1820	0.0500
12	2.40	1.000	2.40	0.1649	0.0450
13	2.70	1.230	2.30	0.0000	0.0000
14	3.20	1.400	2.20	0.2182	0.0700
15	2.80	1.470	2.40	0.1600	0.0500
16	3.20	1.600	2.40	0.1944	0.0600
17	3.50	1.800	2.40	0.0000	0.0000

stacked amplitude averaged over all incident and scattered angles) expressed in explicit decoupled form by using the travel times, amplitudes and polarization vectors of incident and outgoing wave modes. Wavefield separation and regular noise suppression is performed through the use of the polarization projection (Eq. (20)) and special implitude weights (Eqs. (22) and (25)) during the migration process. This process is based on performing the diffraction stack along the Huygens' isochrone $\tau^{(\mu\nu)} = t$ with respect to the subsurface point Q. Eq. (29) is consistent with the principle of elastic-wave PreSDM (Kuo and Dai, 1984): when the decoupled downward continuation is carried out to the point Q at the location of the reflector, the phase of the reflected/transmitted qP- or qS-wave matches that of the direct wave coming from the point R. Therefore, the enhanced images are formed at these locations through the simultaneous migration of qP- and qS-waves. Otherwise, Eq. (29) yields a negligible value.

4.6. Complex-trace migration

In Eq. (29), the remaining cross-talk energy could be due to possible velocity errors or the frequency-dependent ellipticity of the trajectories of the arrival ellipses caused by strong lateral velocity variations. To minimize this energy, each vector trace $\dot{\boldsymbol{u}}_0(S,R,t)$ is converted to the time-domain analytic signal

$$\dot{\boldsymbol{u}}_0(S,R,t) \approx Re[\boldsymbol{a}^{(\mu)}(S,R,t)\dot{u}^{(\mu)}(S,R,t)] \tag{30}$$

similar to its frequency-domain counterpart given by Eq. (3). In the above expression, the instantaneous polarization $\boldsymbol{a}^{(\mu)}(S,R,t)$ and the instantaneous magnitude $\dot{u}^{(\mu)}(S,R,t)$ of the μth wave mode can be expressed in terms of the 3×3 covariance matrix $\mathbf{K}(t)$, as

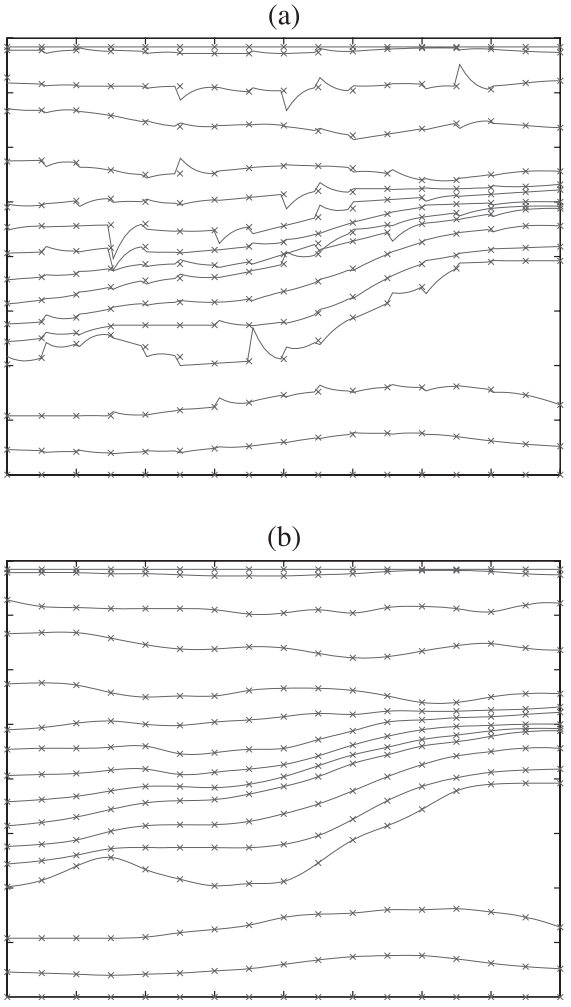

Fig. 2. Original 17×16 (crosses) and interpolated $10^3 \times 16$ (solid lines) Moreni horizon grids: (a) standard cubic spline interpolation from the CWP/SU library of CSM and (b) L2 B-spline fitting (Cheney and Kincaid, 1999).

described by Vidale (1986). When Eq. (30) is used in Eq. (29), the final PreSDM formula becomes

$$K^{(\mu\nu)}(Q) = \frac{4\pi}{A^{(\mu)}(R,Q)} Re \int_{\Sigma_0} \dot{u}^{(\mu)}(S,R,t=\tau^{(\mu\nu)}) \times E^{(\mu\nu)}(S,R,t=\tau^{(\mu\nu)}) G^{(\nu)}(S,Q) \Psi^{(\nu)}(S,Q) \times \Omega^{(\mu\nu)}(Q) \mathrm{d}\sigma(S) \quad (31)$$

with the instantaneous polarization weight

$$E^{(\mu\nu)}(S,R,t) = \left(\boldsymbol{e}^{(\mu)}(S,R,t) \cdot \boldsymbol{e}^{(\nu)}(S) \right) \quad (32)$$

As with semblance weights used in multi-component stacking (Milkereit and Spencer, 1987; Kennett, 2000), the polarization filter $E^{(\mu\nu)}$(Eq. (32)) can help to increase the quality of wavefield separation during PreSDM. Imaging via Alford rotation (Hou and Marfurt, 2002), extrapolation of scalar potentials (Zhe and Greenhalgh, 1997), and the controlled direction reception filtering in ($\tau-p$) space (Greenhalgh et al., 1990) may be regarded as alternative implementations of the projection $E^{(\mu\nu)}$(Eq. (32)). Takahashi (1995) has shown that the weights $\psi^{(\nu)}$, $S2^{(\mu\nu)}$ and $E^{(\mu\nu)}$ (Eqs. (22), (25) and (32)) can largely decrease false images resulting from limited aperture and travel-time errors.

4.7. Final image

According to the elastic migration principle (Kuo and Dai, 1984), the final offset-independent zero-order images $K_0^{(\mu\nu)}$ ($\mu,\nu=1, 2, 3$) in Appendix C should form enhanced intercept/gradient recovery at the depth of the actual reflector Σ' in Fig. 1, i.e. $|K_0^{(\mu\mu)}(Q)| \propto O(1)$ if $Q \in \Sigma'$ and $|K_0^{(\mu\mu)}(Q)| \ll 1$ otherwise. Similarly, the images $K_0^{(\nu\mu)}(Q)$ ($\nu \neq \mu$) should permit enhanced events at the conversion point(s) Q_c, i.e. $|K^{(\nu\mu)}(Q)| \propto O(1)$ if $Q = Q_c$ and $|K^{(\nu\mu)}(Q,R)| \ll 1$ otherwise. This explains the value of using cross-component information in converted-wave imaging.

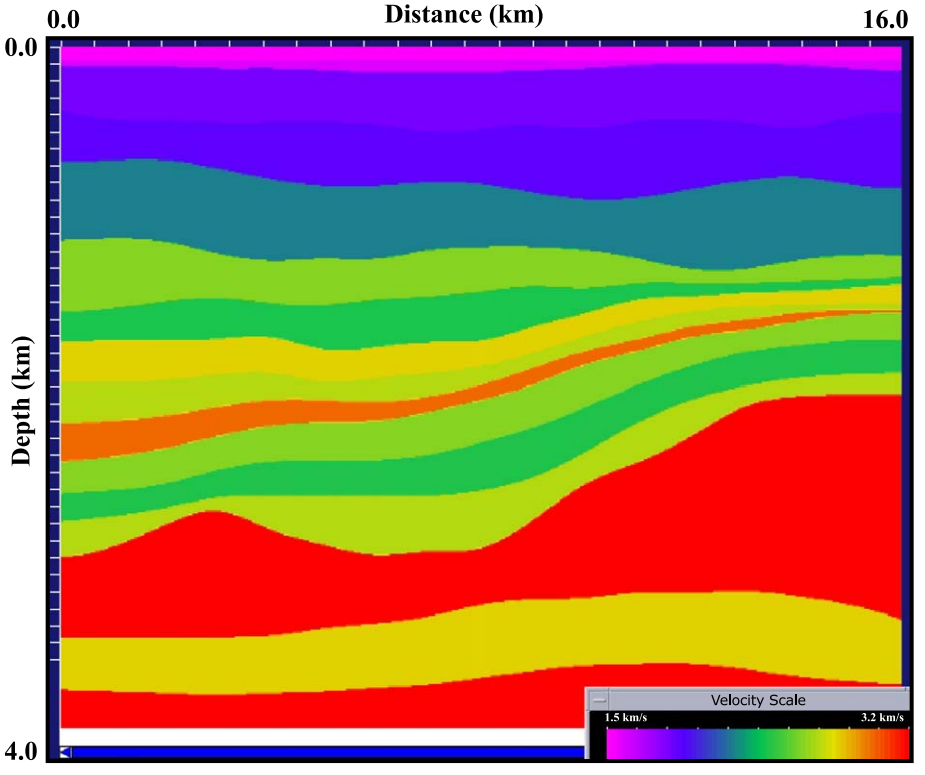

Fig. 3. The Moreni 500 × 500 vertical P-wave velocity grid after 2D L2 B-spline interpolation.

4.8. Marine streamer data

Eq. (31) is also valid for the towed-cable data $u(S,R,t)$. In this case, we set $E^{(\mu\nu)}=1$ to obtain

$$K^{(\mu\nu)}(Q)=\frac{4\pi}{A^{(\mu)}(R,Q)}\int_{\Sigma_0}\dot{u}(S,R,t=\tau^{(\mu\nu)})G^{(\nu)} \times(S,Q)\Psi^{(\nu)}(S,Q)\Omega^{(\mu\nu)}(Q)\mathrm{d}\sigma(S) \quad (33)$$

Assuming an acoustic isotropic medium and a spherical marine source, Hokstad (2000) provides an alternative discussion of this particular case.

4.9. Direct-wave VSP imaging

Let a multi-offset walkaway or reverse VSP survey be configured to give illumination of the target V above the geophone or DHS R for different source or receiver positions S. Although we do not consider downgoing waves at $\Sigma+\Sigma_0$, Eq. (31) is still applicable to backward propagation of transmitted or direct waves between the geophone or DHS datum level Σ and the acquisition surface Σ_0. Here, we explore the similarity between the imaging condition (26) and the so-called excitation-time imaging condition of Chang and McMechan (1986). In the case of direct-wave Pre SDM, Eq. (27) yields the transmission coefficient at the scattering point $Q\in V$. This coefficient is constructed by computing the amplitude of transmitted energy after one-way downward continuation from the surface Σ_0 to the point Q using Eq. (31). In doing so, the transmitted part of the observed wavefield is isolated prior to imaging. The result of downward continuation corresponds to an estimated direct arrival time from the point R. See Chang and McMechan (1986) for details of direct-wave migration.

5. Numerical implementation

5.1. Model building

As with other PreSDM techniques, the present approach implicitly assumes that the input interval velocity model is known. For the sake of simplicity, the focus is on the 2D smooth vertical transverse isotropy (VTI) model to be used in PreSDM. Some

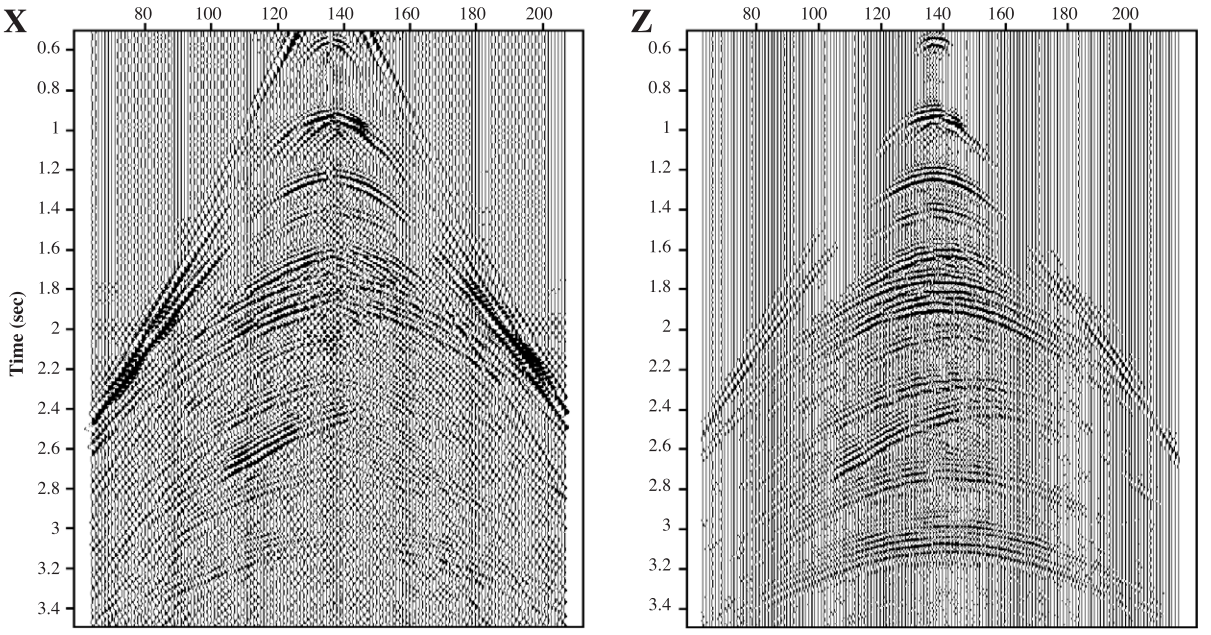

Fig. 4. Common-shot OBC synthetic seismogram (shot 136, trace number versus time): U_x and U_z components of the displacement vector normalized on their maximum values. Data noise is represented by severe aliasing artifacts of the forward modeling algorithm.

considerations on smoothing are discussed by Gajewski et al. (2002). Here, we consider the simple and elegant least-squares (L2) smoothing of geometrical parameters and elastic parameters using B-spline basis functions (Cheney and Kincaid, 1999). The geometrical parameters are represented by densely sampled depth horizon grids after accurate B-spline interpolation of original irregular grids. The elastic parameters are the vertical P-wave velocity v_P, the vertical S-wave velocity v_S, the density ρ, and the Thomsen's (1986) parameters ε, δ, and γ. It is assumed that these parameters may be represented by smoothly varying functions of x and z. Firstly, a special procedure assigns up to 16 spline coefficients to each individual grid rectangle ij. Secondly, the B-spline with continuous first and second derivatives is evaluated at $\{z,x\}$, where $z_i \le z \le z_{i+1}$ and $x_j \le x \le x_{j+1}$. In order to obtain as a smooth surface as possible, we demand the second derivatives to be zero at the boundaries of the model. The present interpolation tool is useful for creating a model grid for finite-difference (FD) modeling, interactive velocity editing and producing a final velocity field consistent with the structure seen on migrated or stacked sections for input to PreSDM.

5.2. Travel time computations

The accurate calculation of the travel time $T^{(v)}(S,Q)$ is important to the success of PreSDM. We compute both FD and ray-trace travel times for the whole model. The Hamiltonian system of kinematic ray equations (Červený, 2001; Hanyga et al., 2001) is solved numerically using the Runge–Kutta method of order $k \ge 2$ (Cheney and Kincaid, 1999). Existing FD eikonal solvers (Podvin and Lecompte, 1991) are used to produce first-arrival travel time maps on the migration grid. Following Coman and Gajewski (2000), later arrivals $T_j^{(v)}(S,Q)$ $(j \ge 1)$ are detected by constructing the KMAH-index map (cf. Appendix D). If KMAH indicates later arrivals we only use ray-trace travel times since we have no FD algorithms to account for singular regions. These travel times are interpolated from ray end points onto the migration grid by B-splines. The eikonal equation is invoked to control errors of ray tracing (Gajewski and Pšencík, 1990; Hanyga et al., 2001). We examine reciprocity $T^{(v)}(S,Q) = T^{(v)}(Q,S)$ to check accuracy of FD travel time computations. The similar considerations apply to the travel time $\tau^{(\mu)}(R,Q)$.

5.3. Amplitude computations

To compute the geometrical spreading (Eq. (A2)), a travel time-based strategy (Gajewski et al., 2002) is implemented. In the present algorithm, this involves the generation of the wavefront curvature attribute, as described by Roberts (2001). See Appendix D for a detail. Also, the dynamic ray tracing system (DRT) is solved by tracing rays through the model over spec-

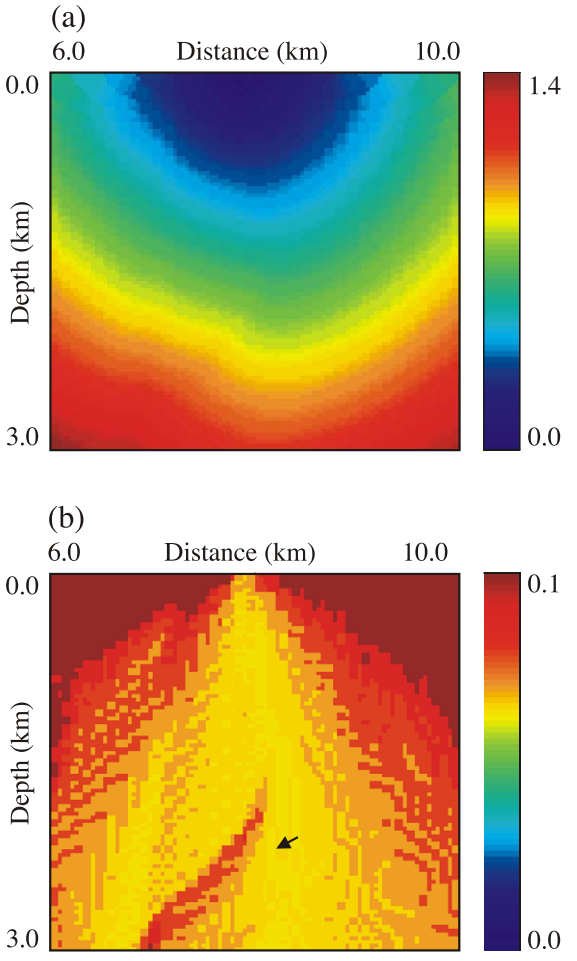

Fig. 5. Example of downgoing qP-wave travel-time and amplitude computations using the first-arrival FD eikonal solver and Eq. (D1) (shot 136): (a) the travel time $\tau^{(1)}(S,Q)$ and (b) the ratio $J^{(1)}(S,Q)/r(S,Q)$. Arrow indicates the region of strong curvature of the rays. The density of rays decreases in this region.

ified range of ray take-off angles according to the ray history code (Gajewski and Pšencík, 1990; Hanyga et al., 2001). We examine the reciprocity relation $G^{(\nu)}(Q,S) = G^{(\nu)}(S,Q)$ to estimate numerical errors of amplitude computations. In Eq. (C5), the amplitude $A^{(\mu)}(R,Q)$ can be expressed in terms of the travel time $\tau^{(\mu)}(R,Q)$ based on a similar strategy.

6. Synthetic example

First, we test the technique on the VTI model "Moreni" provided by Constantin Gerea and Laurence Nicoletis (Institut Français du Pétrole). This realistic anisotropic model simulates a typical marine multi-layered structure with curvilinear interfaces and homogeneous isotropic and VTI layers. The elastic parameters are listed in Table 1. The geometrical parameters are represented by densely sampled horizon grids after spline interpolation of original irregular grids.

Accurate and efficient spatial interpolation is essential for PreSDM. Fig. 2 compares the standard cubic spline interpolation and the L2 B-spline interpolation of the Moreni horizons. Clearly, the L2 B-splines (Fig. 2b) are closer to the exact values than are the standard cubic splines (Fig. 2a). This is because the L2 B-spline interpolation produces the best estimate of any function expressed as a linear combination of spline basis functions. The final velocity model in Fig. 3 consists of 500 × 500 grid cells.

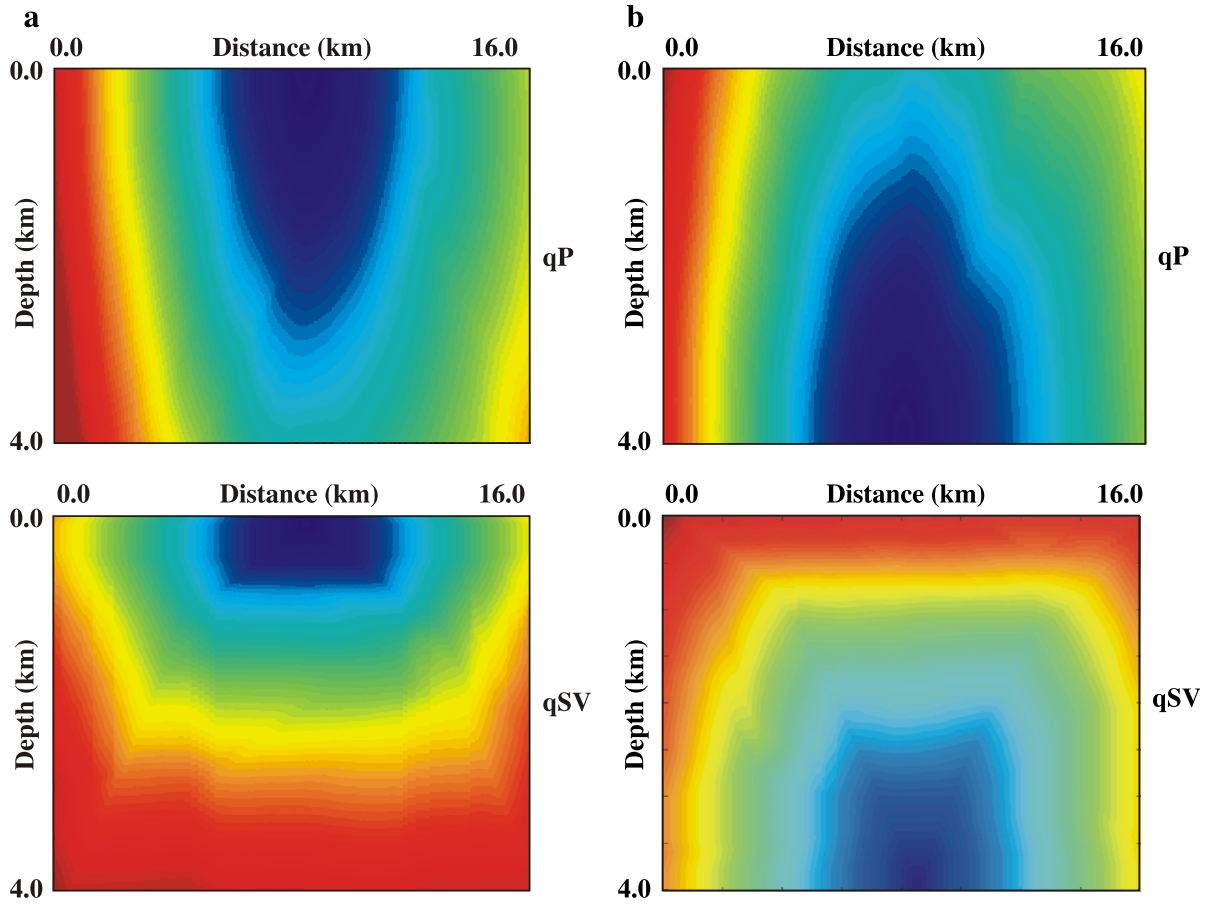

Fig. 6. FD scheme: (a) downgoing and (b) upgoing first-arrival FD travel time computations for qP- and qSV-waves (shot 136). The time scale factor $\tau^{(\nu)}_{\max}$ for $\nu = 1, 3$ is as follows: $\tau^{(1)}_{(\max)} = 4.470$ and $\tau^{(3)}_{(\max)} = 2.884$ (s). The qSV-wave travel-time maps exhibit corner artifacts due to irregular illumination.

The 2D pseudospectral method (Fornberg, 1988) was applied to create a two-component (X–Z) elastic synthetic ocean-bottom cable (OBC) data set (Fig. 4). The corresponding modeling code was provided by Enru Liu of the BGS (original version credited to Huang, 1992). In this example, we study the propagation of qP- and qSV-waves generated by a 30 Hz spherical isotropic source "explosion" ($v,\mu=1,3$). SH-wave propagation ($v=\mu=2$) is not considered. In fact, SH-wave motion is not affected by anisotropy since $\gamma=0$. The data set consists of 256 common-shot gathers with 62.5 m shot spacing. Each common-shot gather consists of 500 receivers with 32 m receiver spacing. The traces are sampled at 3 ms with record length of 7.5 s.

This data set has undergone qP–qP and converted-wave imaging tests based on Eq. (31). In the 2D case, Eq. (31) produces four images as the output of the PreSDM scheme. Common-shot reflectivity images are computed for each pair of incident and outgoing wave modes in order to construct the 2×2 common-receiver scattering matrix

$\begin{pmatrix} K^{(11)} & K^{(13)} \\ K^{(31)} & K^{(33)} \end{pmatrix}$ at the target point Q.

The ray-FD travel-time and amplitude calculation is the most important building block. Reciprocity of travel times $T^{(\nu)}(S,Q)$ and amplitudes $G^{(\nu)}(S,Q)$ is used to estimate the error of Green's function computations due to numerical integration (ray tracing) or numerical differentiation (FD). In doing so, we

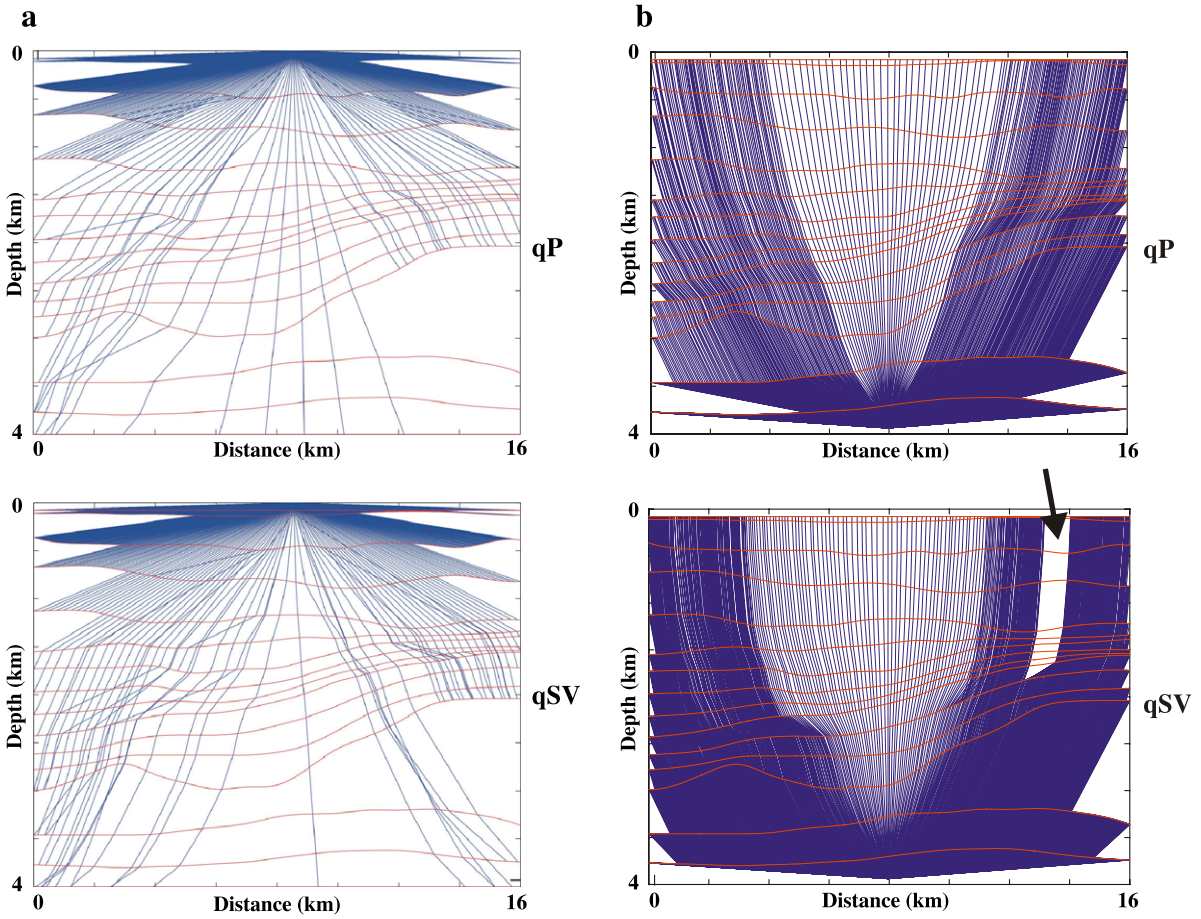

Fig. 7. Ray tracing scheme: (a) downgoing and (b) upgoing initial-value ray tracing for qP- and qSV-waves (sources {8.5, 0.0} and {8.5, 4.0} km). Poor illumination of the downgoing ray tracing is seen. The arrow indicates the shadow zone due to the artifact of B-spline interpolation.

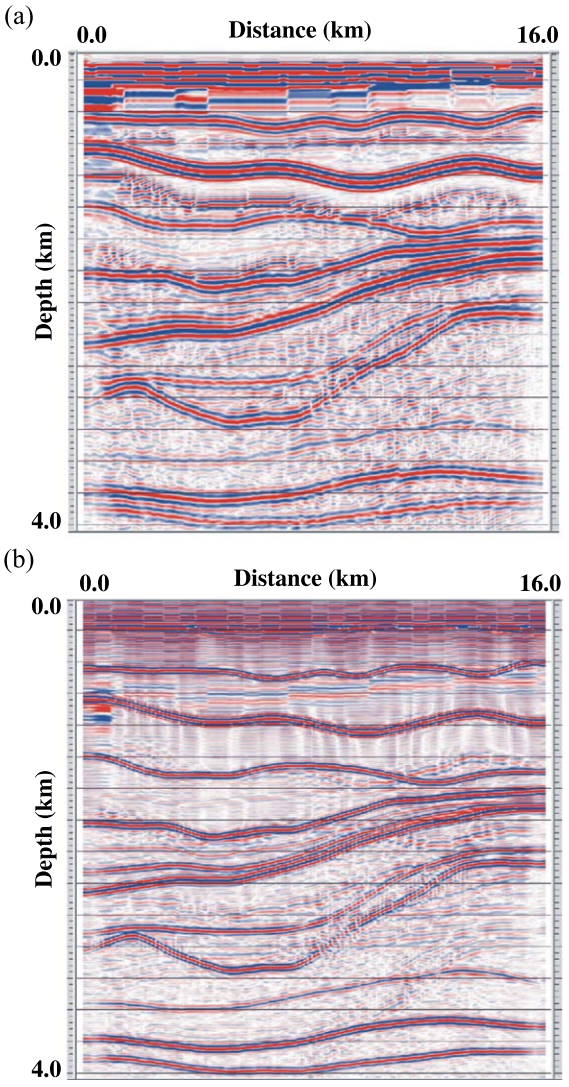

Fig. 8. Results of common-shot PreSDM using Eq. (31) for shots 1–256: (a) qP–qP versus (b) qP–qSV reflectivity sections for the Moreni model in Fig. 3. Data noise has more impact when amplitudes are low. To overcome this instability, a multi-receiver extension of Eq. (31) is required (cf. Appendix C).

compare downgoing and upgoing travel times and amplitudes. Downgoing ray tracing consists of finding all the rays SQ that leave the sources S and propagate through the model. Upgoing rays QS have their termination points at the surface Σ_0. What we get from the differences $T^{(v)}(S,Q) - T^{(v)}(Q,S)$ and $G^{(v)}(S,Q) - G^{(v)}(Q,S)$ are the error estimates prior to spatial interpolation with error control. This guarantees a stable and accurate final output of L2 B-spline interpolation, where the nodes for interpolation are chosen to be the travel-time and amplitude data with error bounds.

In Figs. 5a and 6, the FD travel times of direct downgoing and upgoing qP- and qSV-waves are

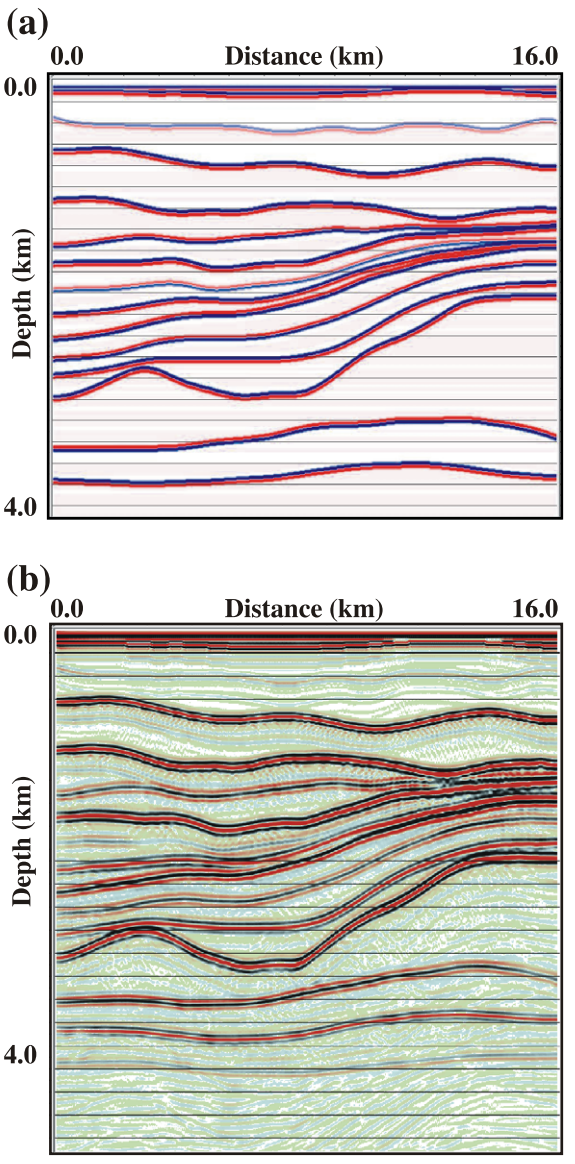

Fig. 9. Example of automated AVA analysis in Appendix C: (a) theoretical qP–qP exploding reflector model (i.e. normal-incidence reflection coefficient convolved with source function) and (b) the angle-independent intercept term $K_0^{(11)}$ estimated from a multi-receiver double diffraction stack (Eq. (C5)) for $\mu = v = 1$.

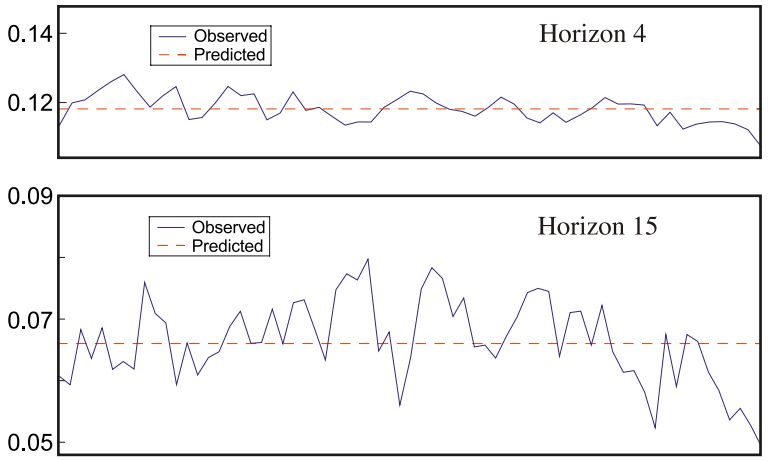

Fig. 10. Comparison of peak instantaneous amplitude values along horizons 4 and 15 in Fig. 9a (dashed line) and b (solid line).

calculated using fast numerical algorithm developed by Linbin Zhang at UC Berkeley. This algorithm extends the explicit FD eikonal solver by Podvin and Lecompte (1991) to VTI media. It is based on the approximate anisotropic dispersion relations obtained by Schoenberg and de Hoop (2000). In contrast to existing anisotropic eikonal solvers (Qian et al., 2001), Zhang's algorithm handles both qP- and qSV-waves. Using Eqs. (D1) and (D2) we can obtain the amplitude (Eq. (A1)). Fig. 5b shows the ratio $J^{(v)}(S,Q)/r(S,Q)$ for qP-wave ($v=1$). As expected, the behaviour of the spreading follows the curvature of the wavefront. Although the present eikonal solver is very efficient, it is necessary to improve on the accuracy of the FD solution by ray tracing, as plotted in Fig. 7. It is seen that the ray tracing method can account for later arrivals near caustics. Also, travel times along ray trajectories can be computed accurately. However, the results of tracing downgoing rays (Fig. 7a) are far from satisfactory due to shadow

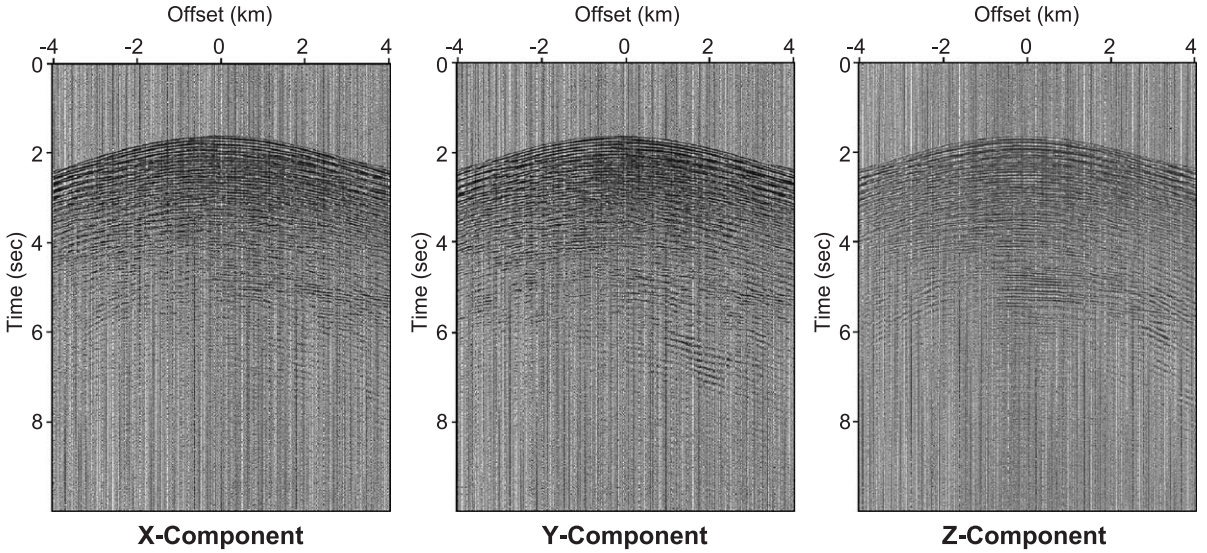

Fig. 11. Three-component field VSP responses corresponding to a walkaway source (courtesy of Phillips Petroleum).

zones. To cure this instability, much more expensive upgoing ray tracing is performed (Fig. 7b). This step is accomplished without absorbing excessive resources by reducing the number of ray segments when rays propagate at small angles to the vertical.

At the final step of the ray-FD algorithm, the L2 B-spline fitting ensures the continuity of interpolated travel times $\tau^{(\mu\nu)}$ and amplitudes $G^{(\nu)}(S,Q)$ as well as the condition of regular illumination. Once this step is completed, travel-time and amplitude tables for each shot point serve as input data to the PreSDM algorithm represented by Eq. (31).

By clustering conventional PCs, this algorithm was implemented in common-shot gathers (Fig. 4). The overall execution time required by PreSDM was quite reasonable. It took about 16 h of CPU time on a 16-node PC cluster to compute the depth images $K^{(11)}$ and $K^{(31)}$ in Fig. 8. Although numerical errors due to forward modeling and insufficient illumination of common-shot migration cause distortion of the migrated waveforms (especially for layers 2 and 12), it appears that both images are in satisfactory agreement with the velocity model in Fig. 3. Fig. 8a identifies primary qP−qP reflections and some multiples; there are almost no multiples in Fig. 8b. Also, the converted-wave image shows higher vertical resolution and better overall signal-to-noise ratio than the qP−qP image, particularly at shallow depths.

In elastic models, improved resolution of converted-wave depth imaging is due to the fact that $\lambda^{(1)}>\lambda^{(2,3)}$, $\lambda^{(\nu)}$ being the wavelength of the νth wave mode. This is consistent with previous results (Dillon et al., 1988; Hokstad, 2000). However, it is well known from practical experience that the higher resolution, theoretically to be expected from shear waves, is often not obtained due to the greater attenuation usually associated with this mode of propagation.

For the angle-dependent migrated sections in Fig. 8, relatively high amplitudes along the shallow reflectors are more likely because of the larger range

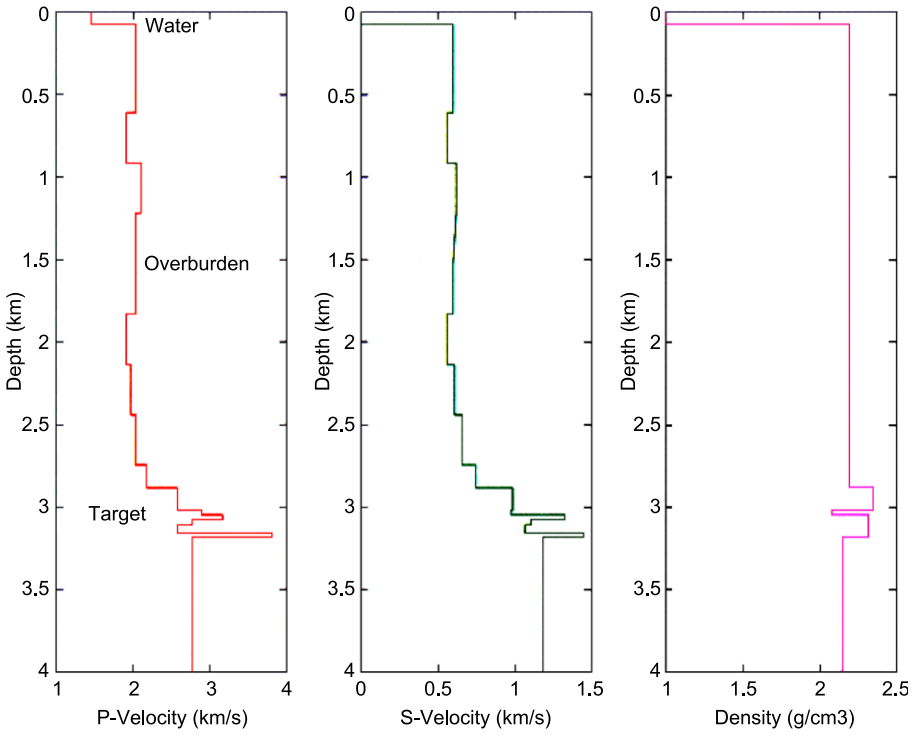

Fig. 12. The initial model for PreSDM of the WVSP data in Fig. 11. This model is the result of standard velocity analysis of surface seismic data constrained by log data after upscaling (courtesy of Phillips Petroleum).

of reflection angles. To obtain angle-independent depth sections of the AVA intercept or gradient terms, a multi-receiver double diffraction stack of common-shot image gathers should be applied, as discussed in Appendix C. For example, the signals which are used in the multi-receiver PreSDM for $\mu = \nu = 1$ are primary qP−qP reflections corresponding to the exploding reflector depth model in Fig. 9a. Fig. 9b shows that Eq. (C8) for $\mu = \nu = 1$ attenuates the wave modes $\mu,\nu \neq 1$ and gives the intercept term $K_0^{(11)}$ which is hardly distinguishable from the theoretical image in Fig. 9a. Fig. 10 depicts the peak instantaneous amplitudes along selected reflectors in Fig. 9b. It is seen that these amplitudes are in fact estimates of the actual normal-incidence qP−qP reflection coefficient. Severe aliasing of input traces, errors in the numerical Green's function computations and aperture effects cause these estimates to be scattered around the exact value. Mean errors are less than 6% and 10% for horizons 4 and 15, respectively. This indicates that the estimate of the intercept term is sufficiently accurate. The estimate is more smooth and accurate for shallow horizons than for deep horizons. The estimate for small (weak-contrast) intercept terms yields a less accurate result.

7. Application to VSP data

Conventional mixed-mode VSP migration (Dillon et al., 1988) is inevitably distorted by inaccuracies of wavefield separation prior to imaging. Therefore, the most reliable test for decoupled PreSDM is processing of raw WVSP data without any attempt to filter with respect to wave mode at the pre-processing stage. The WVSP data set considered here was acquired in a well located in the North Sea. The well is known to intersect the top of the target at approximately 2.8 km depth. Fig. 11 is a three-component common-geophone record. The distance between source posi-

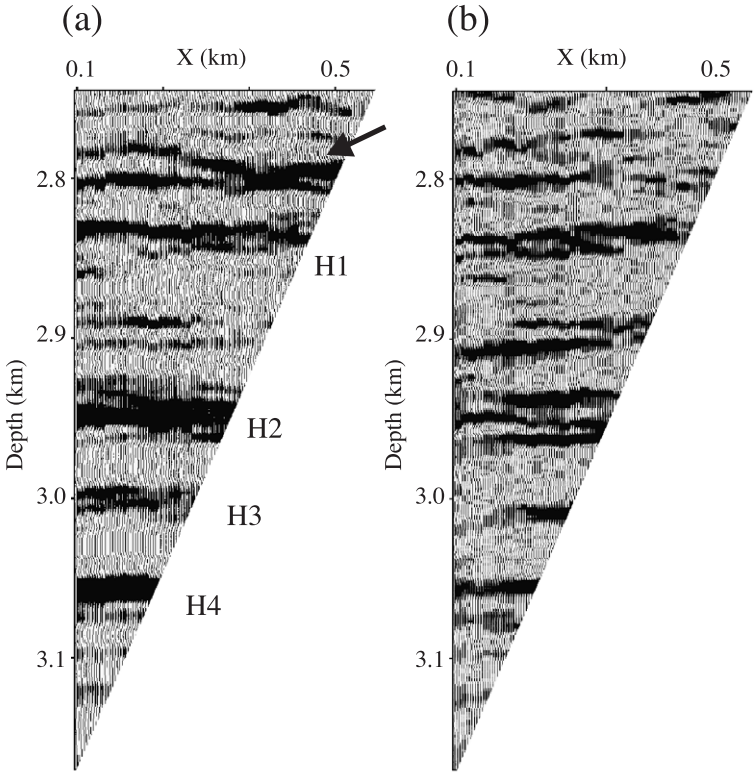

Fig. 13. Decoupled direct-wave WVSP isotropic PreSDM: fragments of (a) PP and (b) PS migrated transmission energy within the zone of optimal illumination above the geophone level. Arrow indicates unremoved free-surface PP multiples.

tions is 25 m. The total length of the line is 8 km. The geophone is located at 3.170 km depth below the midpoint of the line. The initial velocity model in Fig. 12 was suggested by the contractor who had processed the surface seismic data.

Fig. 13 shows isotropic direct-wave depth images of the target zone $z = 2.8–3.1$ km above the geophone level. According to Chang and McMechan (1986), we obtain an image at any (stationary refraction) point along the direct ray based on an argument that incoming scattered and direct rays have different directions. The reconstruction of the transmission coefficient is accomplished by back propagating and decoupling downgoing waves using Eq. (31). Both PP-wave and converted-wave (PS) images tie well with major geologic horizons H1–H4 in the domain of interest (Fig. 13). As in the previous example, we observe that the shear-wave image exhibits a somewhat shorter wavelength than the PP-wave image for the same bandwidth of input data in Fig. 11.

The final test is carried out for the target zone $z = 3.65–4.05$ km below the geophone level by back propagating and decoupling upgoing PP and shear waves. The 0.1×0.4 km target is placed close to the borehole within the locus of reflection points for the converted-wave energy. The results are shown in Fig. 14 and agree with those of Dillon et al. (1988). Even though there is not a perfect one-to-one correspondence between the migrated events in Figs. 14a and b, it is apparent that converted-waves form a noticeably better image of the principal reflectors R1–R4 than P-waves.

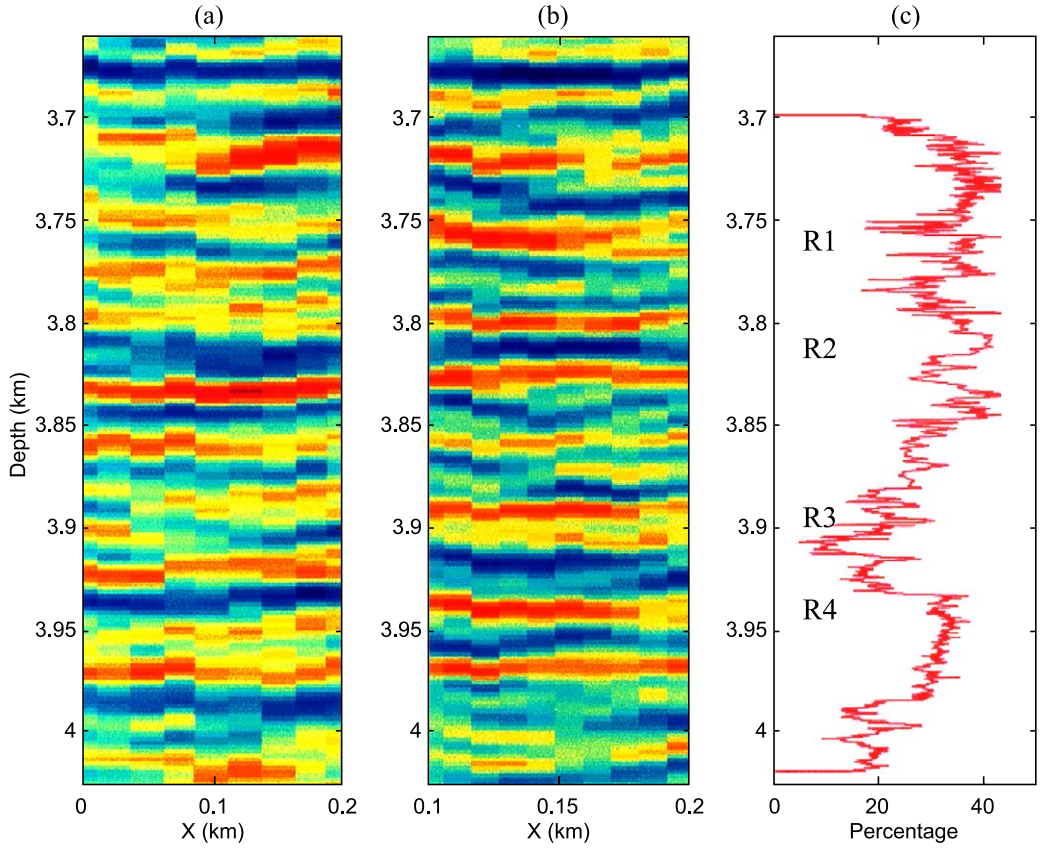

Fig. 14. Decoupled WVSP isotropic PreSDM with upgoing waves: normalized PP, PS reflectivity sections (decoupled WVSP isotropic PreSDM) and porosity map (log data) versus depth below the target zone in Fig. 12. Maximum and minimum values of normalized reflectivities are 1 and −1.

8. Discussion and conclusion

The elastic imaging algorithm is simple to implement by migrating the displacement vector without wavefield separation at the pre-processing stage. In this paper, a rigorous vector migration formula represented in an explicit decoupled form has been derived and successfully tested. This technique is based on the stationary-phase principle applied to the elastic Green's theorem. Compared with previous treatments, the new formula contains wave mode decomposition filters representing certain polarization and arrival-angle weights. The present work and previous results (Takahashi, 1995) demonstrate that these weights can decrease migration artifacts significantly, yielding good estimates of reflection coefficients. We have shown how robust angle independent AVA attributes may be constructed from these estimates using the double diffraction stack technique outlined in Appendix C. The final formula (Eq. (31)) is suitable for migration of both multi-component (e.g. OBC, VSP) and conventional marine seismic data with the commonly used scalar algorithms developed for PP PreSDM. Hence, the approach is easy to implement and eliminates the assumption that the reflected PP wave is best represented on the vertical component, whereas the reflected PS wave is the strongest on the horizontal component. We have developed a ray-FD approach that incorporates fast first-arrival FD eikonal solvers and ray tracing algorithms into a single framework. We have chosen this approach to generate accurate Green's function travel time and amplitude maps. Amplitudes are computed in terms of travel times (cf. Appendix D). It is possible to consider irregular regions, i.e. later arrivals. All input quantities are computed from coarsely gridded tables using an accurate L2 B-spline interpolation tool. A new imaging condition implicitly assumes that (a) the input velocity model is known and (b) there is no confusion of wave modes (e.g. kiss singularity). Despite the fact that the proposed method relies on the modeled and observed polarizations of wavefields, numerical results are encouraging and show that the quality of decoupled imaging does not depend strongly on the cross-component noise. The method is particularly useful in situations where different wave modes have orthogonal polarizations. The numerical algorithm allows elastic PreSDM to be done inexpensively on PC-based distributed memory clusters. A more comprehensive AVA analysis and migration of noisy data with incorrect velocity models will be the subject of a future study.

Acknowledgements

This work was funded by the Edinburgh Anisotropy Project (EAP) at the British Geological Survey (BGSNERC) and is published with the permission of the Executive Director of the BGS and the EAP sponsors: Agip, BG, BP, Chevron-Texaco, CNPC, Conoco Phillips Exxon Mobil, KerrMcGee, Landmark, Marathon, Schlumberger, Norsk Hydro, PGS, Trade Partners UK, Total and Veritas DGC. Numerical modeling and FD eikonal solver codes were provided by Enru Liu (BGS). I thank Peter Bakker (Shell) and Claudia Vanelle (Hamburg University) for their careful review and helpful suggestions in revising the paper. Thanks go to Xiang-Yang Li (BGS) for supporting this research. I also thank Brian Bainbridge (BGS) for his help in Linux software maintenance and MPI programming. My sincere appreciation is extended to Russ Evans (BGS) for his constructive remarks.

Appendix A. Green's function amplitude

The zeroth-order ray approximation (Chapman and Coates, 1994) of the Green's function amplitude $G^{(\nu)}(S,Q)$ along the ray that connects the source S to the target point Q is

$$G^{(\nu)}(S,Q) = \frac{1}{4\pi}\frac{\exp[-i\pi\ sign(\omega)\chi^{(\nu)}(S,Q)/2]}{\sqrt{\rho(S)v^{(\nu)}(S)\rho(Q)v^{(\nu)}(Q)J^{(\nu)}(S,Q)}} + O\left(\frac{1}{\omega}\right), \quad \text{(A1)}$$

where $\chi^{(\nu)}(S,Q)$ is the KMAH index (which takes into account possible caustics) and $J^{(\nu)}(S,Q)=J^{(\nu)}(Q)/J^{(\nu)}(S)$ is the relative geometrical spreading factor for the νth wave mode calculated by dynamic ray

tracing (Gajewski and Pšencík, 1990; Hanyga et al., 2001). In this notation, the absolute geometrical spreading factor is given by

$$J^{(v)}(S) = \left|([\partial_1 \boldsymbol{x}^{(v)}(S) \times \partial_2 \boldsymbol{x}^{(v)}(S)] \cdot \boldsymbol{l}^{(v)}(S))\right|, \quad \text{(A2)}$$

where $\boldsymbol{l}^{(v)}$ is the unit ray direction vector and $\partial_\alpha \boldsymbol{x}^{(v)}(S) = \partial \boldsymbol{x}^{(v)}(S)/\partial \varsigma_a$ is the partial derivative of the ray position vector $\boldsymbol{x}^{(v)}$ with respect to the ray parameter ς_a ($a = 1,2$) representing the ray take-off angle. Instead, other authors (Ben-Menahem et al., 1991; Červený, 2001; Schleicher et al., 2001) use the following geometrical spreading factor

$$L^{(v)}(S) = J^{(v)}(S)\sec\,\psi^{(v)}(S) \quad \text{(A3)}$$

where $\psi^{(v)} = \cos^{-1}(c^{(v)}/v^{(v)})$ is the angle between the phase normal and the ray direction vector ($0 \le \psi^{(v)} < \pi/2$) and $c^{(v)}$ denotes the phase velocity.

Appendix B. Relation to Zoeppritz coefficient

To establish the analytic relationship between the migrated image (Eq. (26)) and the Zoeppritz coefficient $K^{(\mu v)}(Q) = K^{(\mu v)}(Q;S_0)$ at the specular (reflection/transmission) point S_0, the zeroth-order ray approximation (Červený, 2001) is applied to the incident wave

$$u^{(\mu)}(R,Q) = \Lambda\, A^{(\mu)}(R,Q)\exp[i\omega\tau^{(\mu)}(R,Q) + i\chi + i\pi sign(\omega)\chi^{(\mu)}(R,Q)/2] \quad \text{(B1)}$$

and to the recorded wavefield

$$\begin{aligned} u^{(v)}(S,R,\omega) &= \Lambda F_0(\omega) A^{(\mu)}(R,Q) K^{(\mu v)}(Q;S) A^{(v)}(Q,S) \\ &\quad \times \exp\{i\omega[\tau^{(\mu)}(R,Q) + \tau^{(v)}(Q,S)] \\ &\quad + i\pi sign(\omega)[\chi^{(\mu)}(R,Q) + \chi^{(v)}(Q,S)]/2\} \end{aligned} \quad \text{(B2)}$$

Here, Λ is the source directivity (Gajewski, 1993), $\exp(i\chi) = F_0(\omega)/F(\omega)$ is the source phase shift, $\chi^{(\mu)}(R,Q)$ and $\chi^{(v)}(Q,S)$ are, respectively, the numbers of caustics (KMAH index) along the ray paths RQ and QS, and $A^{(\mu)}(R,Q)$ and $A^{(v)}(Q,S)$ are the corresponding ray-theory amplitudes. Moreover, the ray-theory amplitude $A^{(v)}(Q,S)$ may be written as (Hanyga et al., 2001)

$$A^{(v)}(Q,S) = \sqrt{\frac{\rho(Q)v^{(v)}(Q)J^{(v)}(Q)}{\rho(S)v^{(v)}(S)J^{(v)}(S)}} \quad \text{(B3)}$$

with the absolute geometrical spreading factor specified by Eq. (A2). As a result, substituting Eqs. (A1 and B (1–3) into Eq. (26) and taking into account Eqs. (22), (25), and (28) we obtain

$$I^{(\mu v)}(Q,0) = \partial_t f(0) D^{(\mu v)}(Q), \quad \text{(B4)}$$

where

$$D^{(\mu v)}(Q) = \int_{\Sigma_0} K^{(\mu v)}(Q;S)\cos\alpha^{(\mu v)}(Q)\cos\theta^{(v)}(S)\mathrm{d}\sigma(S) \quad \text{(B5)}$$

Since the magnitude of the window function $\cos\alpha^{(\mu v)}(Q)$ decreases as the distance $r(S,S_0)$ increases and $\alpha^{(\mu v)} = 0$ at the specular point S_0, the integral (B5) can be approximately evaluated as

$$D^{(\mu v)}(Q) \approx K^{(\mu v)}(Q;S_0)\cos\theta^{(v)}(S_0) \quad \text{(B6)}$$

Here, the weighting factor $\cos\theta^{(v)}(S_0)$ has useful implications at far offsets. Also, it accounts for the curvature of the surface Σ_0. In the case of land observations configured on an almost flat horizontal surface Σ_0, we may often set $\cos\theta^{(v)}(S_0) \approx 1$.

Appendix C. Migration AVA analysis

Let us introduce the ray parameter p corresponding to the ray path RQ. For the sake of simplicity, we may set $p = \partial_1 \tau^{(\mu)}(R,Q)$. The AVA technique is to expand the reflection/transmission coefficient in Eq. (29) in a Taylor series in the parameter p

$$K^{(\mu v)}(p) = K_0^{(\mu v)} + K_1^{(\mu v)} p + K_2^{(\mu v)} p^2 + O(p^3) \quad \text{(C1)}$$

with the angle-independent coefficients $K_n^{(\mu v)}$ expressed in terms of the elastic parameters $\rho(Q)$ and $\mathbf{C}(Q)$ (for stratified isotropic media, see Ursin and Dahl, 1992). Substituting Eq. (C1) into Eq. (29) and integrating (stacking) over the current point R of the receiver acquisition surface Σ_R (the sea floor in OBC the borehole axis in VSP or the streamer cable),

we obtain

$$B^{(\mu\nu)} = K_0^{(\mu\nu)} P_0 + K_1^{(\mu\nu)} P_1 + K_2^{(\mu\nu)} P_2 + O(p^3), \quad \text{(C2)}$$

where

$$P_n = \int_{\Sigma_R} p^n \mathrm{d}\sigma(R), \qquad n \geq 0, \quad \text{(C3)}$$

$$B^{(\mu\nu)} = \int_{\Sigma_R} \{\mathrm{d}\sigma(R) \times \frac{4\pi}{A^{(\mu)}(R,Q)} \int_{\Sigma_0} \left(\partial_t \boldsymbol{u}_0[S,R,t=\tau^{(\mu\nu)}] \cdot \boldsymbol{e}^{(\nu)}(S)\right) \times G^{(\nu)}(S,Q) \Psi^{(\nu)}(S,Q) \Omega^{(\mu\nu)}(Q) \mathrm{d}\sigma(S)\} \quad \text{(C4)}$$

or, using Eq. (31),

$$B^{(\mu\nu)} = \int_{\Sigma_R} \{\mathrm{d}\sigma(R) \frac{4\pi}{A^{(\mu)}(R,Q)} Re \int_{\Sigma_0} \dot{u}^{(\mu)}(S,R,t=\tau^{(\mu\nu)}) \times E^{(\mu\nu)}(S,R,t=\tau^{(\mu\nu)}) G^{(\nu)}(S,Q) \times \Psi^{(\nu)}(S,Q) \Omega^{(\mu\nu)}(Q) \mathrm{d}\sigma(S)\} \quad \text{(C5)}$$

Solving the linear system (C2) yields the offset-independent depth images $K_n^{(\mu\nu)}$. Note that these images are obtained after a double summation operation. In principle, they are dependent on the range of acquisitions Σ_0 and Σ_R (aperture effects).

If the reflector is a symmetry plane for the class of anisotropy considered and $\mu,\nu = 1, 2, 3$, Eq. (C1) takes the following form (for isotropy, see Ursin and Dahl, 1992)

$$K^{(\mu\nu)}(p) = \begin{cases} K_0^{(\mu\nu)} + K_1^{(\mu\nu)} p^2 + K_2^{(\mu\nu)} p^4 + O(p^6) & \mu = \nu \\ p[K_0^{(\mu\nu)} + K_1^{(\mu\nu)} p^2 + K_2^{(\mu\nu)} p^4] + O(p^6) & \mu \neq \nu \end{cases} \quad \text{(C6)}$$

Hence

$$B^{(\mu\nu)} = \begin{cases} K_0^{(\mu\nu)} P_0 + K_1^{(\mu\nu)} P_2 + K_2^{(\mu\nu)} P_4 + O(p^6) & \mu = \nu \\ K_0^{(\mu\nu)} P_1 + K_1^{(\mu\nu)} P_3 + K_2^{(\mu\nu)} P_5 + O(p^6) & \mu \neq \nu \end{cases} \quad \text{(C7)}$$

For a limited range of incidence angles ($|p| \ll 1$), the system (C7) yields

$$K_0^{(\mu\nu)} \approx \begin{cases} B^{(\mu\nu)}/P_0 & \mu = \nu \\ B^{(\mu\nu)}/P_1 & \mu \neq \nu \end{cases} \quad \text{(C8)}$$

Conventionally, this solution is referred to as either the intercept term for nonconverted waves ($\mu = \nu$) or the gradient term for converted waves ($\mu \neq \nu$).

Appendix D. Travel-time based amplitude computations

Let the FD travel-time map $\tau(x,y,z)$ be calculated in a gridded form. This means that the simple nearest-neighbour search can be used to generate the set of wavefront surfaces (isochrones) $\tau(x,y,z) = \mathrm{t}$ within the time range $[\tau_{\min}, \tau_{\max}]$. In order to calculate the slowness vector $\boldsymbol{p}(x,y,z)$ and the Gaussian wavefront curvature $K_G(x,y,z)$, a local least-squares quadratic approximation to each wavefront is applied using the surrounding grid values on this surface (after Roberts, 2001). The slowness vector can be expressed in terms of the dip-angle and azimuth attributes; the orientation of any normal curvature may also be estimated (Roberts, 2001). When the slowness vector **p** is known, it is a straightforward matter to compute the polarization vector $\boldsymbol{e}$ and the group velocity vector $\boldsymbol{v}$ based on the plane-wave theory (Červený, 2001). The geometrical spreading J can be defined as

$$J \approx K_G^{-1} \frac{\Delta\phi_1}{\Delta\zeta_1} \frac{\Delta\phi_2}{\Delta\zeta_2} \cos\psi, \quad \text{(D1)}$$

with the angle $\phi_{1,2}$ being the orientation of the principal curvature and $\cos\psi = c/v$ (cf. Appendix A). Here, $\Delta\zeta_{1,2}$ are the perturbations of the slowness vector along the principal directions of the minimum wavefront surface $\tau(x,y,z) = t_{\min}$ surrounding the source, whereas $\Delta\phi_{1,2}$ are the perturbations of the slowness vector along the principal directions of the current wavefront surface $\tau(x,y,z) = t_{\min}$. Note that the geometrical spreading defined in terms of the travel-time map $\tau(x,y,z)$ should not vanish near ray singularities since the FD eikonal solvers rarely produce shadow zones.

Finally, the difference in the KMAH index χ between the two adjacent wavefronts $\tau(x,y,z)=t$ and $\tau(x,y,z)=t+\Delta t$ can be written as

$$\chi(t+\Delta t)-\chi(t)=\Delta\chi_1+\Delta\chi_2, \qquad \text{(D2)}$$

where $\Delta\chi_{1,2}=\begin{cases}1 & s_{1,2}=-1\\ 0 & s_{1,2}=1\end{cases}$,

$s_{1,2}=\text{sign}\{\boldsymbol{n}_{1,2}(t)\cdot\boldsymbol{n}_{1,2}(t+\Delta t)\}$ and $\boldsymbol{n}_{1,2}(t)$ is the unit vector that specifies the principal direction of the wavefront surface $\tau(x,y,z)=t$. An edge-type display of the KMAH-index map is very effective at delimiting caustic geometries. When the radius of wavefront curvature is very small or zero, this also indicates that the ray path belongs to a caustic.

References

Ben-Menahem, A., Gibson Jr., R.L., Sena, A.G., 1991. Green's tensor and radiation patterns of point sources in general anisotropic inhomogeneous elastic media. Geophys. J. Int. 107, 297–308.

Bleistein, N., 1984. Mathematical Methods for Wave Phenomena. Academic Press.

Červený, V., 2001. Seismic Ray Theory. Cambridge Univ. Press.

Chang, W.-F., McMechan, G.A., 1986. Reverse-time migration of offset vertical seismic profiling data using the excitation-time imaging condition. Geophysics 51, 67–84.

Chapman, C.H., Coates, R.T., 1994. Generalized Born scattering in anisotropic media. Wave Motion 19, 309–341.

Cheney, W., Kincaid, D., 1999. Numerical Mathematics and Computing. Brooks/Cole Publishing, Pacific Grove, CA.

Coman, R., Gajewski, D., 2000. 3-D multivalued traveltime computation using a hybrid method. 70th Ann. Internat. Mtg, Soc. of Expl. Geophys., pp. 2309–2312.

Dillon, P.B., Ahmed, H., Roberts, T., 1988. Migration of mixed mode VSP wavefields. Geophys. Prospect. 36, 825–846.

Docherty, P., 1991. A brief comparison of some Kirchhoff integral formulas for migration and inversion. Geophysics 56, 1164–1169.

Druzhinin, A., Pedersen, H., Campillo, M., Kim, W., 1998. Elastic Kirchhoff–Helmholtz synthetic seismograms. Pure Appl. Geophys. (PAGEOPH) 151, 17–45.

Gajewski, D., 1993. Radiation from point sources in general anisotropic media. Geophys. J. Int. 113, 229–317.

Gajewski, D., Pšencík, I., 1990. Vertical seismic profile synthetics by dynamic ray tracing in laterally varying layered anisotropic structures. J. Geophys. Res. 95, 11301–11316.

Gajewski, D., Coman, R., Vanelle, C., 2002. Amplitude preserving Kirchhoff migration: a traveltime based strategy. Stud. Geophys. Geod. 46, 193–211.

Greenhalgh, S.A., Mason, I.M., Lucas, E., Pant, D., Eames, R.T., 1990. Controlled direction reception filtering of P- and S-waves in ($\tau-p$) space. Geophys. J. Int. 100, 221–234.

Fornberg, B., 1988. The pseudospectral method: accurate representation of interfaces in elastic wave calculations. Geophysics 53, 625–637.

Hanyga, A., Druzhinin, A.B., Dzhafarov, A.D., Frøyland, L., 2001. A Hamiltonian approach to asymptotic seismic reflection and diffraction modeling. Geophys. Prospect. 49, 213–227.

Hokstad, K., 2000. Multicomponent Kirchhoff migration. Geophysics 65, 861–873.

Hou, A., Marfurt, K.J., 2002. Multicomponent prestack depth migration by scalar wavefield extrapolation. Geophysics 67, 1886–1894.

Kennett, B.L.N., 1984. Reflection operator methods for elastic waves: II. Composite regions and source problems. Wave Motion 6, 419–429.

Kennett, B.L.N., 2000. Stacking three-component seismograms. Geophys. J. Int. 141, 263–269.

Kuo, J.K., Dai, T-.F., 1984. Kirchhoff elastic wave migration for the case of noncoincident source and receiver. Geophysics 49, 1223–1238.

Milkereit, B., Spencer, C., 1987. A new migration method applied to the inversion of P–S converted phases. In: Worthington, M.H. Deconvolution and Inversion. Blackwell, Oxford, pp. 251–266.

Mittet, R., Hokstad, K., 1995. Transforming walkaway VSP data into reverse VSP data. Geophysics 60, 968–977.

Podvin, P., Lecompte, I., 1991. Finite difference computation of travel times in very contrasted velocity models: a massively parallel approach and its associated tools. Geophys. J. Int. 105, 271–284.

Qian, J., Symes, W., Dellinger, J., 2001. A full-aperture anisotropic eikonal solver for quasi-P traveltimes. 71st Ann. Internat. Mtg, Soc. of Expl. Geophys., pp. 129–132.

Reiter, E.C., Toksöz, M.N., Keho, T.H., Purdy, G.M., 1991. Imaging with deep-water multiples. Geophysics 56, 1081–1086.

Roberts, A., 2001. Curvature attributes and their application to 3D interpreted horizons. First Break 19.2, 85–100.

Schleicher, J., Tygel, M., Ursin, B., Bleistein, N., 2001. The Kirchhoff–Helmholtz integral for anisotropic elastic media. Wave Motion 34, 353–364.

Sena, A.G., Toksöz, M.N., 1993. Kirchhoff migration and velocity analysis for converted and nonconverted waves in anisotropic media. Geophysics 58, 265–276.

Schoenberg, M.A., de Hoop, M.V., 2000. Approximate dispersion relations for qP–qSV-waves in transversely isotropic media. Geophysics 65, 919–933.

Takahashi, T., 1995. Prestack migration using arrival angle information. Geophysics 60, 154–163.

Thomsen, L., 1986. Weak elastic anisotropy. Geophysics 51, 1954–1966.

Tygel, M., Schleicher, J., Hubral, P., Hanitzsch, C., 1993. Multiple weights in diffraction stack migration. Geophysics 59, 1820–1830.

Ursin, B., Dahl, T., 1992. Seismic reflection amplitudes. Geophys. Prospect. 40, 483–512.

Vidale, J.E., 1986. Complex polarization analysis of particle motion. Bull. Seismol. Soc. Am. 76, 1393–1405.

Wapenaar, C.P.A., Berkhout, A.J., 1989. Elastic Wave Field Extrapolation Elsevier, Amsterdam.

Zhe, J., Greenhalgh, S.A., 1997. Prestack multicomponent migration. Geophysics 62, 598–613.